Spin dynamics simulation of polarization transfer in spin-exchange optical pumping

Bachelor's thesis

Marko Tuomela

Physics degree program
Faculty of science
University of Oulu

June 9, 2020

Contents

Chapter 1

Introduction

NMR spectroscopy offers us tools to study the structure of different materials. For its non-invasive quality, NMR is especially beneficial in the study of biological matter. Since the electromagnetic waves utilized in spectrometers are in the radio wave frequency range, samples can be examined for long periods without harm. However, the achieved NMR signal is relatively weak. The strength of NMR signal is determined by the net magnetization of a sample, which emerges from occupational differences in nuclear spin states. This difference is normally only a few spins per million. With certain methods, we can increase this difference in nuclear spin states favorably, which we call hyperpolarization. One of these hyperpolarization techniques is called spin-exchange optical pumping (SEOP) [1]. SEOP is a method of spin polarizing noble-gas nuclei in gas-phase collisions with optically polarized alkali-metal atoms, yielding a far greater NMR signal.

The SEOP technique has not yet been completely exhausted. In terms of finding optimal conditions for spin polarization transfer to occur, quantitative analysis is the key. As a computational approach, a multi-scale simulation combining molecular dynamics, quantum chemistry and spin dynamics was created [2]. This method allows microscopic investigation of individual gas-phase collision events between the alkali-metal and noble-gas atoms. In the preceding iteration of this work, microscopic molecular and spin dynamics occurring in Rb-Xe SEOP experiment were simulated. The chosen simulation conditions allowed the study of the polarization transfer from the unpaired electron of the ^{85}Rb atom to the ^{129}Xe nucleus in a Rb-Xe gas mixture at a vanishing external magnetic field along with static temperature and pressure. The experimental trends of polarization transfer were reproduced with reasonable accuracy, while the rate of polarization transfer showed heavy overestimation possibly due to the unrealistic Rb number density [3].

In this work, we have taken steps in order to address the questions left behind in the previous study. A more refined python code for spin dynamics was created to allow changes for more versatile analysis of the microscopic behavior of the Rb-Xe transfer.

Further additions in the spin Hamiltonian, such as the Rb hyperfine coupling to its own nucleus, were included to more realistically represent the interactions at play in the polarization transfer. For a more encyclopedic study, we incorporated the ability to change the isotopes of Rb and Xe in the gas composition. However, new molecular dynamics trajectories were not calculated due to the small percentual mass difference of $^{129/131}$Xe and $^{85/87}$Rb.

Beside these additions, the refined multi-scale simulation operated in accordance to its predecessor. Molecular dynamics simulation of the atomic trajectories were calculated as a function of time at set temperature and pressure, followed with quantum-chemical calculations to obtain the instantaneous parameters of the spin Hamiltonian, and finally extracting the relevant spin transfer via spin dynamics simulation driven by the propagation of the spin system.

The simulation provided both expected and unforeseen results when changes were introduced in noble-gas isotopes and interaction parameters. The difference in polarization transfer of the Xe isotopes showed accordance with previous research of the case, while the roles played by long-lived van der Waals complexes and short binary collisions revealed important insight on the maximum optimal length of an interaction event. The results showed an increase in the rate of polarization transfer as the lifetime of the event grew longer until a certain point, where the transfer started to decline. This implies that there seems to be a limit on the optimal duration of an interaction event. Further research on the matter is required.

Chapter 2

Theory

2.1 Nuclear magnetic resonance

All of the information in chapters 2.1, 2.1.1, 2.1.2 and 2.2 are from sources [4, 5].

Nuclear magnetic resonance (NMR) arises from the interaction between magnetic atomic nuclei and external magnetic fields. This phenomenon yields us a method with versatile applications in several fields of science, known as NMR spectroscopy, offering valuable information on physical, chemical and biological properties of matter. The best known practice of NMR spectroscopy is unquestionably magnetic resonance imaging (MRI), used widely in medical science. While the well-known X-ray imaging shows us harder substances, such as bones, MRI can reveal the soft tissue. The significant benefit of this method is its non-invasive nature. Samples can be studied without harming them as the radiation used for the irradiation of the sample is non-ionizing, meaning the photons lack the energy needed to completely separate an electron from an atom or a molecule.

In short, NMR spectroscopy is the study of external magnetic fields affecting the orientation of the nuclear magnetic moments of atomic nuclei. However, a significant shortcoming of NMR is the achievable NMR signal strength. The conventional signal strength is proportional to thermal polarization, which is around the magnitude of 10^{-5}. We will delve in this with greater detail later. While some atomic nuclei experience the NMR phenomenon well, others do not experience it at all. This originates from a property we call spin.

2.1.1 Spin

Spin is a fundamental property of an atom, such as are the electric charge and mass. Spin is a quantum-mechanical property that, for our purposes, can be described much like a spinning top. The direction of its axis of rotation determines the orientation of

the particle in question.

Spin is quantized, meaning it appears in multiples of $\pm 1/2$. Individual unpaired particles, such as protons, neutrons and electrons all carry a spin of $1/2$. From this quantization we can comprehend that atomic nuclei compose a system of multiple nucleons, which can only possess a discrete spin quantum number $I = n \cdot 1/2$, where $n = 0, 1, 2, 3 \ldots$, and the spin's projection $(-I, -I+1, \ldots, I-1, I)$ changes the values accordingly. A net zero nuclear spin can be achieved if two or more particles have spins of opposite signs and pair up to eliminate the manifestation of spin. A non-zero nuclear spin causes the nucleus to have a spin angular momentum $\boldsymbol{I}$, a vector quantity with direction as well as magnitude, of which the latter can be described as

$$|\boldsymbol{I}| = \sqrt{I(I+1)}\hbar. \tag{2.1}$$

Here, and henceforth in this thesis, I refers to the spin quantum number of the nucleus and S to the spin quantum number of the electron, with the possible values of $I = 0, \frac{1}{2}, 1, \frac{3}{2}, \ldots$ and $S = \frac{1}{2}$. We are particularly interested in the component of $\boldsymbol{I}$ that is oriented parallel with the external magnetic field $\boldsymbol{B}$. This is usually chosen to be I_z

$$I_z = \hbar m \ ; \ m = I, I-1, I-2, \ldots, -I, \tag{2.2}$$

where m can have $(2I+1)$ values. We can see that the magnitude of I_z is always less than that of $\boldsymbol{I}$, meaning that the spin of the particle is never perfectly oriented along the z-axis.

If a nucleus possesses a non-zero spin angular momentum, it also has a magnetic moment $\boldsymbol{\mu}$, which is parallel to $\boldsymbol{I}$, in the same direction or the opposite

$$\boldsymbol{\mu} = \gamma\hbar\boldsymbol{I}. \tag{2.3}$$

The z-component of the magnetic moment is

$$\mu_z = \gamma\hbar I_z = \gamma\hbar m, \tag{2.4}$$

where the coefficient γ is a variable that is unique to every nucleus, called the gyromagnetic ratio. It describes the degree of magnetic moment of the nucleus in question.

2.1.2 Energy levels

To understand how a particle with non-zero nuclear spin behaves in an external magnetic field, we need to consider its spin as a magnetic moment vector. In the external field, the magnetic moment acts like a magnet with north and south poles, aligning itself parallel to the field. However, $2I+1$ possible orientations for the particle exist

within this parallelism, some being low- and some high-energy states. These energy configurations depend on the sign of the gyromagnetic ratio. When $\gamma > 0$, the low-energy orientation is $\boldsymbol{I} \uparrow\uparrow \boldsymbol{B}$, and $\boldsymbol{I} \uparrow\downarrow \boldsymbol{B}$ when $\gamma < 0$.

According to classical physics, the interaction between a magnetic moment $\boldsymbol{\mu}$ and magnetic field $\boldsymbol{B}$ will apply a torque to the magnetic dipole while possessing a potential energy

$$E = -\boldsymbol{\mu} \cdot \boldsymbol{B}. \tag{2.5}$$

This is known as the Zeeman interaction. If the magnetic field is oriented along the z-axis, according to the equation (2.4), the Zeeman interaction simplifies into

$$E = -\gamma \hbar B m. \tag{2.6}$$

We can see that the energy values of the states are also quantized.

The particle can shift between the energy states by absorbing or emitting a photon of energy equal to the energy difference between the two spin states. Only the transitions from an energy level to another with $\Delta m = \pm 1$ are directly observable, so the energy needed for a shift is

$$\Delta E = \pm \gamma \hbar B. \tag{2.7}$$

Photon's energy can be described as $E = h\nu$, where the variable ν is known as the resonance frequency. The frequency of the photons used to produce these energy level transitions is

$$\nu = \frac{\Delta E}{h} = \frac{\gamma \hbar}{h} B = \frac{\gamma}{2\pi} B. \tag{2.8}$$

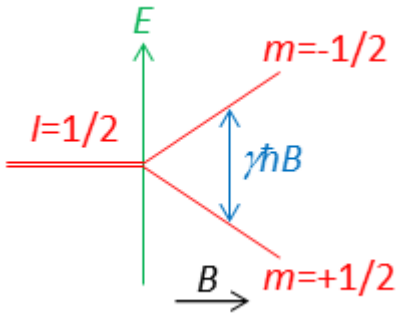

Figure 2.1: Energy level diagram of a particle in an external magnetic field in the case of $I = 1/2$ and $\gamma > 0$, where m refers to the spin state of the particle. $+1/2$ and $-1/2$ refer to the low- and high-energy states, respectively [4].

2.2 Nuclear spin polarization

When a system of spins, such as a group of atomic nuclei, is placed in an external magnetic field, each of the spins aligns itself in the field according to the $2I+1$ possible orientations. In the case of $I = 1/2$ and $\gamma > 0$, we will denote spin up ($m_I = +1/2$) as the low-energy state and spin down ($m_I = -1/2$) as the high-energy state. It is important to note that according to quantum mechanics, the measured orientation of the spin states is never exactly aligned with the external magnetic field (Eq. 2.2). For example the angle between vectors $\boldsymbol{I}$ and $\boldsymbol{B}$ for spin-up ($I = 1/2$) nucleus is 54.7°.

However, due to thermal energy, all nuclei are not in the lower energy spin-up state. In room temperature the thermal energy kT is far greater than the energy difference ΔE between the states, which leads to a nearly equal spin configuration with only a very small occupation difference between spin-up and spin-down states. These state population numbers obey Boltzmann statistics, and the ratio of identical spin $1/2$ nuclei is

$$\frac{N_{-1/2}}{N_{+1/2}} = e^{-\Delta E/kT}. \tag{2.9}$$

It is evident that changes in temperature or magnetic field affect the ratio of the population of the spin states. The difference between the lower and higher energy states is normally in the order of 10^{-5}.

When we take a look into a system of multiple nuclei, we see that the net magnetic moment of the system is the sum of its individual nuclear magnetic moments. The occupation difference between the spin states causes the system to possess a macroscopic nuclear magnetization, which can be described in thermal equilibrium as

$$M_0 = \frac{N\gamma^2\hbar^2 I(I+1)}{3kT} B_0, \tag{2.10}$$

where N refers to the number of identical nuclei in the system. The observable NMR signal received from a sample is directly proportional to this nuclear magnetization, which can be increased by raising the magnitude of the external magnetic field or by decreasing temperature.

Now we can see that NMR spectroscopy is heavily reliant on the populus contrast between the spin-up and spin-down states. Devising this difference in spin populations is what we call nuclear spin polarization.

2.2.1 Hyperpolarization

There are techniques that allow us to produce non-equilibrium nuclear spin polarization [6], which can be in order of unity in ambient conditions. This is known as hyperpo-

larization. With these methods we can increase the degree of polarization far beyond thermal equilibrium, thus greatly enhancing the signal in NMR studies. In this thesis we will focus on one of these techniques with greater detail.

2.2.2 Spin-exchange optical pumping

Spin-exchange optical pumping is one of several hyperpolarization methods. It allows effective polarization of magnetic noble-gas nuclei via the process of gas-phase collisions with spin-polarized alkali-metal atoms. This polarization is typically five orders of magnitude greater than the achievable thermal polarization [1]. Although any alkali-metal is eligible for this method, rubidium is the most convenient because its high vapor pressure allows operation under modest temperatures [1]. Moreover, noble gases are preferred for hyperpolarization, since their sufficiently long T_1 relaxation times enable transportation from the hyperpolarizer to the detection zone [7]. While ^{3}He has had a prominent role in hyperpolarization experiments, there is a simple reason why the noble-gas of choice nowadays is xenon; it is a renewable resource with relatively high natural abundance and low cost [7]. More specifically, it has more benefits found in its high solubility, especially in biomedical science. In this thesis we use rubidium for our alkali metal and xenon for our noble gas.

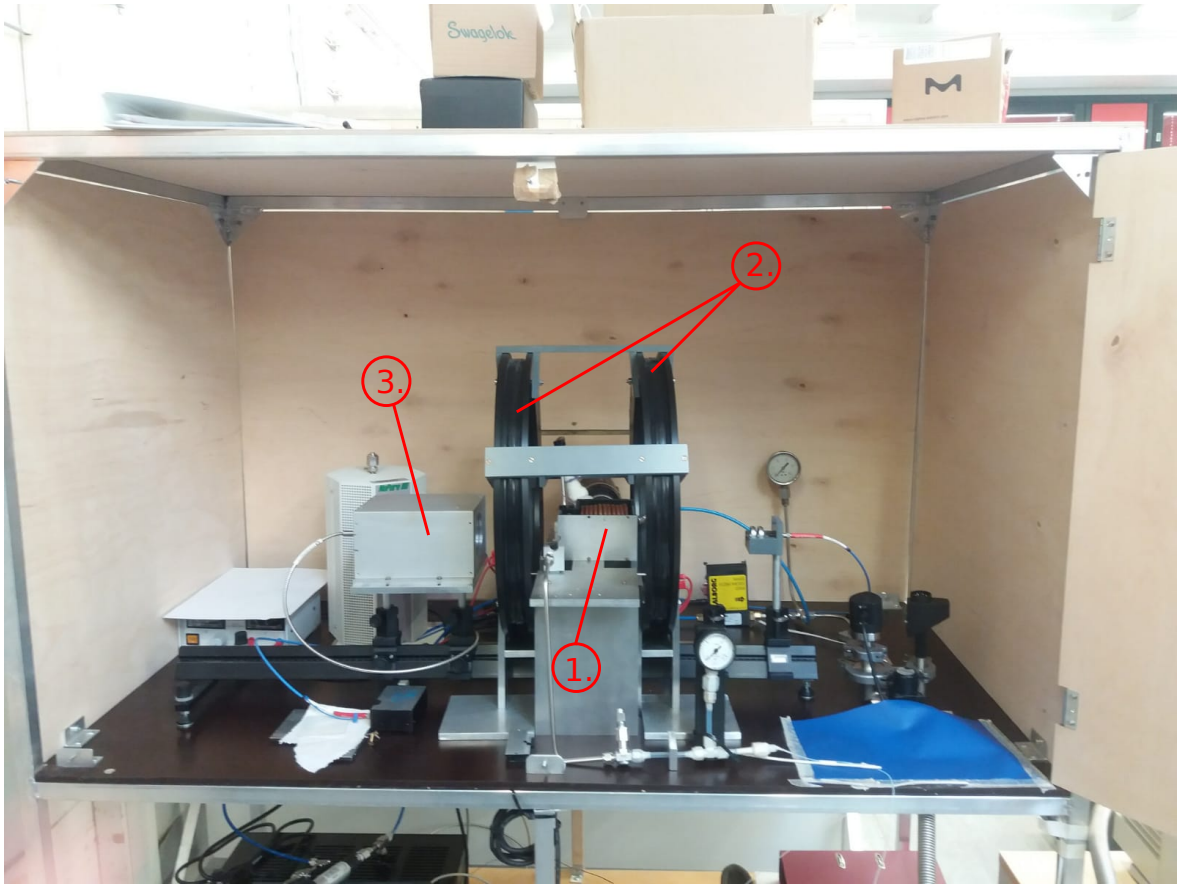

Figure 2.2: Picture of experimental SEOP arrangement. Alkali-metal atoms, noble-gas atoms and nitrogen used as a quenching gas flow into a glass cell in different phases of the experiment. (1) The cell is placed in an oven which allows the alkali-metal to enter vapor phase. (2) It is surrounded by coils which allow the generation of z-axis oriented magnetic field. (3) A laser light is used to illuminate the cell to allow alkali-metal spin polarization through optical pumping. The credit of creating this arrangement goes to Anne Selent.

Continuous illumination with circularly polarized light is used to optically pump the rubidium atoms in order to induce an energy level shift. The light is of resonant frequency with the transition from the ground electronic state $^2S_{1/2}$ to the first excited state $^2P_{1/2}$. This is called a D_1 transition. The light excites the alkali-metal atoms from $^2S_{1/2}$ spin down ($m_S = -1/2$) state to the $^2P_{1/2}$ spin up ($m_J = +1/2$) state. The spin population of the excited states of the alkali-metal quickly equalizes by colliding with the noble-gas atoms. Re-population of ground states ensues through quenching collisions with the nitrogen (N_2) molecules[1] with nearly equal probability of relaxing to $m_S = \pm 1/2$ [1].

Through this process the average density of spin angular momentum of rubidium electrons changed from -1/2 units before the photon absorption to 0 units after being quenched back to ground state, so on average 1/2 units of spin angular momentum is

[1]Nitrogen exists in the arrangement as a quenching gas, suppressing the re-radiation of light as a source of relaxation.

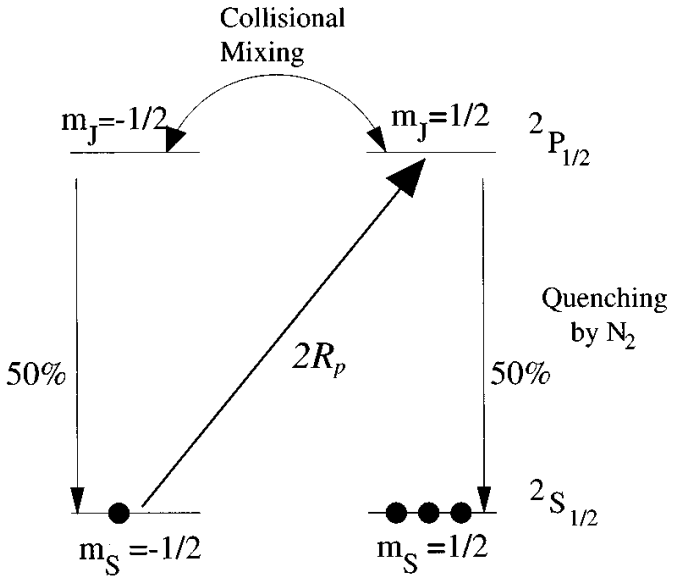

Figure 2.3: Diagram of the alkali-metal atoms interacting with circularly polarized light. Source: [1].

deposited in the vapor for each absorbed photon [1].

The crucial step is the collisional spin-exchange between the rubidium atoms and xenon nuclei. There are two main types of collisions where this exchange occurs, fast binary collisions and the formation of long-lived van der Waals molecules. The ratio of these two collision types is determined by gas pressure, where greater pressures reduce the formation probability of the longer van der Waals complexes. The spin polarization transfer is dominated by binary collisions for lighter atoms, such as ^{3}He, while in the case of heavier noble gases like ^{129}Xe with substantially lesser gas pressures, the contribution of van der Waals molecules can vastly exceed the transfer granted by binary collisions [1].

2.3 Spin Hamiltonian

Spin Hamiltonian is essentially a model composed of all the interactions affecting the system, whether internal or external. It is a model in the sense that it enables parametrization of experimental data into a sum of terms. The spin Hamiltonian contains operators of the electron and nuclear spins, external magnetic field and other interacting entities, along with interaction parameters that tie the entities together. These parameters exist in the form of 2-index tensors [8].

Eigenfunctions of the spin Hamiltonian determine the possible energy levels of the system. Thus it is effectively an expression of energy, where the degrees of freedom for the system are composed in the equation explicitly and implicitly. For example, the electron and nuclear spin operators are chosen in the equation as visibly separate, explicit entities, while other degrees of freedom, such as the nuclear and electron positions are held within the tensors implicitly [8].

The interacting explicit components relevant to our spin Hamiltonian are the effective electron spin $\hat{\boldsymbol{S}}$, nuclear spin $\hat{\boldsymbol{I}}$, external magnetic field $\boldsymbol{B}$ and the rotational angular momentum of the Rb-Xe pair, $\boldsymbol{M}$:

$$\hat{H}(t) = \mu_B \hat{\boldsymbol{S}} \cdot \boldsymbol{g}(t) \cdot \boldsymbol{B} + \hat{\boldsymbol{S}} \cdot \boldsymbol{\epsilon}(t) \cdot \boldsymbol{M} + \hat{\boldsymbol{S}} \cdot \boldsymbol{A}_{\mathrm{Xe}}(t) \cdot \hat{\boldsymbol{I}}_{\mathrm{Xe}} + \hat{\boldsymbol{S}} \cdot \boldsymbol{A}_{\mathrm{Rb}}(t) \cdot \hat{\boldsymbol{I}}_{\mathrm{Rb}}. \quad (2.11)$$

The interaction parameters, or tensors, of the spin Hamiltonian are typically gathered from quantum-chemical calculations and/or interpretation of experimental results [2], which we will go through in the order of appearance. The first term containing the g-tensor, $\boldsymbol{g}(t)$, is the electron Zeeman term. It describes the interaction between the electron spin and the external magnetic field. The second term with the epsilon tensor, $\boldsymbol{\epsilon}(t)$, is the interaction between electron spin and rotational angular momentum of the Rb-Xe pair. In this work, it is approximated from the g-tensor [9]. The final two terms are hyperfine interactions, $\boldsymbol{A}_{\mathrm{Xe}}(t)$ and $\boldsymbol{A}_{\mathrm{Rb}}(t)$, describing the coupling between the Rb electron and Xe/Rb nucleus. The last term is only included in certain parts of the upcoming results [2].

2.4 Time-dependent Schrödinger equation

According to quantum mechanics, position and momentum cannot be used to describe the movement of particles in the atomic scale, since these properties can only be known with certain probability instead of well-known trajectory. That is why we use the wave function $\Psi(\boldsymbol{r}, t)$ to describe the state of the particle instead of Newton's laws. To describe the time evolution of these states, we use the Schrödinger equation

$$i\hbar\frac{\partial}{\partial t}\Psi(\boldsymbol{r},t) = \Big(-\frac{\hbar^2}{2m}\nabla^2 + V(\boldsymbol{r},t)\Big)\Psi(\boldsymbol{r},t), \tag{2.12}$$

where ∇^2 is the Laplacian. The Schrödinger equation is analogous to Newton's second law ($F = ma$) in the sense that the initial value $\Psi(\boldsymbol{r},0)$ together with the equation determines the position- and time-evolution of the wave function $\Psi(\boldsymbol{r},t)$ [10].

Another popular form of the time-dependent Schrödinger equation is

$$i\hbar\frac{d}{dt}\left|\Psi(t)\right\rangle = \hat{H}\left|\Psi(t)\right\rangle \tag{2.13}$$

where $\hat{H}$ is the Hamiltonian operator [11]. In short, it is the representation of a time-evolving system.

2.4.1 Liouville-von Neumann equation

In quantum mechanics, the state of a specific quantum system is depicted by a state vector $|\psi(t)\rangle$ [10]. If a system cannot be written as a combination of multiple states but has a state vector, it is called a pure state. More specifically, pure quantum states correspond to vectors in Hilbert space. Now instead of a single state vector describing the system, it can be in different states $|\psi_i(t)\rangle$ with different probabilities q_i. In other words, we have a pure state ensemble $\{q_i, |\psi_i(t)\rangle\}_i^N$, which can be written as

$$\hat{\rho}(t) = \sum_i q_i \left|\psi_i(t)\right\rangle \left\langle\psi_i(t)\right|. \tag{2.14}$$

This is called the density operator, and is equivalent to the pure state ensemble. It is essentially a statistical state of the system, which can used to calculate the probabilities for outcomes of well-defined measurements [11].

While the Schrödinger equation characterizes the time evolution of pure states, the Liouville-von Neumann equation is used to describe the time evolution of a density operator. They are in fact equivalent, as either of the equations can be derived from another.

The dynamics of a projection operator $\hat{\rho}(t) = |\psi(t)\rangle\langle\psi(t)|$ satisfies the Liouville-von Neumann equation

$$\begin{aligned}
&\frac{d\hat{\rho}(t)}{dt} = \frac{d}{dt}(|\psi(t)\rangle\langle\psi(t)|) = \frac{d|\psi(t)\rangle}{dt}\langle\psi(t)| + |\psi(t)\rangle\frac{d\langle\psi(t)|}{dt} \\
&= -\tfrac{i}{\hbar}\hat{H}(t)|\psi(t)\rangle\langle\psi(t)| + |\psi(t)\rangle\langle\psi(t)|\tfrac{i}{\hbar}\hat{H}(t)^\dagger \\
&= -\tfrac{i}{\hbar}\hat{H}(t)\hat{\rho}(t) + \tfrac{i}{\hbar}\hat{\rho}(t)\hat{H}(t) = -\tfrac{i}{\hbar}[\hat{H}(t),\hat{\rho}(t)] = \hat{L}(t)\hat{\rho}(t)
\end{aligned} \tag{2.15}$$

where the projection operator $\hat{\rho}(t)$ is that of an arbitrary spin system. The final density operator is achieved by averaging these projection operators.

Physical observables, such as momentum or position are represented in quantum

mechanics by operators. For example, the previously mentioned Hamiltonian operator is an expression of energy. We define the Liouvillian superoperator acting on operator $\hat{c}$ as

$$\hat{\hat{L}}(t)\hat{c} = -\frac{i}{\hbar}[\hat{H}(t), \hat{c}], \tag{2.16}$$

where the von Neumann equation dictates a condition [11]

$$\frac{d\hat{\rho}(t)}{dt} = \hat{\hat{L}}(t)\hat{\rho}(t), \tag{2.17}$$

which can be derived from the Schrödinger equation for the local spin system state $|\psi(t)\rangle$ [2].

Chapter 3

Research

3.1 Objectives and questions

The main objective of this thesis is to approach the spin polarization transfer from alkali-metal electrons to noble-gas nuclei (Rb→Xe) from a computational standpoint. The ability to analyze the polarization transfer quantitatively is key in the optimization of the SEOP technique. Our method of approach is a multi-scale simulation with the capability of adding or removing interaction parameters of the spin Hamiltonian. We can also examine the effect that different isotopes of the noble gas or alkali metal have on the rate of polarization transfer. The closer inspection of how collision duration affects the rate of polarization transfer will ultimately lead to the possibility of optimization of gas pressure, temperature and composition for SEOP experiments.

3.1.1 Different isotopes

While the more abundant ^{129}Xe is well-studied, the quadrupolar isotope ^{131}Xe has received far less attention in NMR spectroscopy. It is the only other stable and NMR-active isotope of this noble gas, with a spin quantum number of $I = 3/2$ and natural abundance of 21.2%, compared to ^{129}Xe spin quantum number and natural abundance of $I = 1/2$ and 26.4%, respectively [12].

If the spin quantum number of a nucleus is greater than $1/2$ (meaning $I \geq 1$), the nucleus is quadrupolar. Its electric charge distribution is not spherically symmetric and in addition to magnetic fields, electric field gradients can also cause a torque to the nucleus, changing its orientation [4].

How does this quadrupolar ^{131}Xe isotope behave in terms of spin-exchange?

3.1.2 Hyperfine coupling

The coupling of electron and nuclear spins is known as hyperfine interaction. The two main contributions to this interaction are the isotropic Fermi contact and the anisotropic spin-dipolar hyperfine interactions [2, 8].

The two final spin Hamiltonian terms (Eq. 2.11) represent this interaction, where $\boldsymbol{A}(t)$ is the hyperfine tensor. The former hyperfine term describes the interaction of rubidium electron spin and xenon nuclear spin, while the latter the hyperfine coupling of rubidium electron spin to its own nuclear spin, which has not been included in former iterations of this research. What is the impact on polarization transfer when the coupling $\hat{\boldsymbol{S}} \cdot \boldsymbol{A}_{\mathrm{Rb}}(t) \cdot \hat{\boldsymbol{I}}_{\mathrm{Rb}}$ is added to the spin Hamiltonian?

3.1.3 Collision duration and rate of exchange

As mentioned before, spin polarization transfer results from interaction events between the two entities. Two extremes of these interaction events are the fast binary collisions and the formation of long-lived van der Waals complexes. For heavier noble gases, such as ^{129}Xe, the contribution of van der Waals molecules seem to dominate the polarization transfer. However, the ratio of binary versus van der Waals collisions can be manipulated with gas pressure [1]. A closer look into the rate of polarization transfer can give us insight into optimizing the ratio of these two species of collisions to develop hyperpolarization in the SEOP technique.

3.2 Methods

While a considerable amount of experimental work has been done, quantitative microscopical analysis of spin polarization transfer still remains largely undone. Moreover, finding and rationalizing the optimal conditions of gas pressure and temperature are intriguing for experimental physicists. We have approached this matter via a computational basis. The novelty of this method lies in the ability of microscopic investigation of individual collision events, which is yet to be studied.

3.2.1 Computational

As our approach we have established a multi-scale simulation method combining molecular dynamics (MD), quantum chemistry (QC) and spin dynamics (SD) to simulate the spin polarization transfer from the unpaired electrons of the alkali-metal (Rb) atoms to the noble-gas (Xe) nuclei, as well as relaxation processes, from first principles.

A new stand-alone implementation of the SD simulation in Python language was created to demonstrate this approach by simulating the spin polarization transfer from

Rb electrons to Xe nuclei in gas-phase collision events between the two species [13].

The method is based on the sampling of a MD trajectory by QC calculations to first-principles compute the parameters of the spin Hamiltonian. Using the spin Hamiltonian, time propagation of the spin density matrix can be achieved numerically by solving the Liouville-von Neumann equation [3, 13, 14].

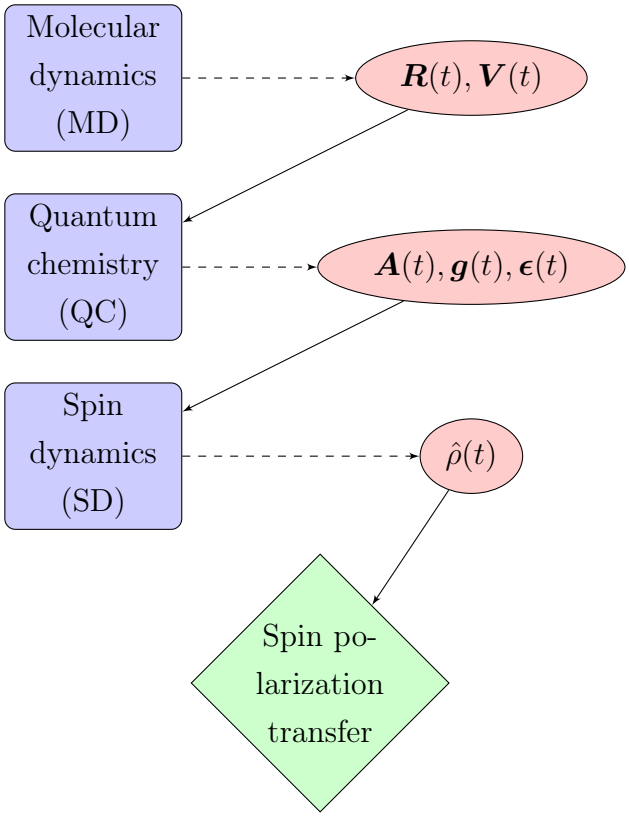

Figure 3.1: Diagram of the multi-scale simulation structure.

The instantaneous positions $\boldsymbol{R}(t)$ and velocities $\boldsymbol{V}(t)$ of the atoms are retrieved from a MD simulation trajectory, which in turn is obtained by the integration of the classical equations of motion [2]. They are then used in QC calculations to form the interaction parameters handled in the spin Hamiltonian.

The size of the spin system is determined by the base electron spin and nuclear spin operators ($\hat{\boldsymbol{S}}$, $\hat{\boldsymbol{I}}$). For example, the electron spin operator $\hat{\boldsymbol{S}} = (\hat{S}_x, \hat{S}_y, \hat{S}_z)$, where the relevant z-oriented component and its unity operator are

$$\hat{S}_z = \begin{pmatrix} \frac{1}{2} & 0 \\ 0 & -\frac{1}{2} \end{pmatrix}, \; \hat{E}_S = \begin{pmatrix} 1 & 0 \\ 0 & 1 \end{pmatrix}. \tag{3.1}$$

In a spin system that consists of electron spin as well as nuclear spin, the operators transform to correspond the new size as

$$\begin{aligned} \hat{S}_z &\rightarrow \hat{E}_I \otimes \hat{S}_z \\ \hat{I}_z &\rightarrow \hat{I}_z \otimes \hat{E}_S, \end{aligned} \tag{3.2}$$

where the $\hat{I}_z$ and $\hat{E}_I$ refer to the nuclear spin operator z-component and its unity operator, as was for the electron spin. In the case of ^{129}Xe nucleus ($I = 1/2$) and Rb electron ($S = 1/2$), the components are

$$\hat{E}_I = \begin{pmatrix} 1 & 0 \\ 0 & 1 \end{pmatrix} \; ; \; \hat{S}_z = \begin{pmatrix} \frac{1}{2} & 0 \\ 0 & -\frac{1}{2} \end{pmatrix}, \tag{3.3}$$

and the outer product opens up as

$$\hat{E}_I \otimes \hat{S}_z = \begin{pmatrix} \hat{S}_z & 0 \\ 0 & \hat{S}_z \end{pmatrix} = \begin{pmatrix} \frac{1}{2} & 0 & 0 & 0 \\ 0 & -\frac{1}{2} & 0 & 0 \\ 0 & 0 & \frac{1}{2} & 0 \\ 0 & 0 & 0 & -\frac{1}{2} \end{pmatrix}. \tag{3.4}$$

In the case of ^{131}Xe ($I = 3/2$) and Rb electron spin ($S = 1/2$), we have the components

$$\hat{E}_I = \begin{pmatrix} 1 & 0 & 0 & 0 \\ 0 & 1 & 0 & 0 \\ 0 & 0 & 1 & 0 \\ 0 & 0 & 0 & 1 \end{pmatrix} \; ; \; \hat{S}_z = \begin{pmatrix} \frac{1}{2} & 0 \\ 0 & -\frac{1}{2} \end{pmatrix}, \tag{3.5}$$

and the outer product establishes a form of

$$\hat{E}_I \otimes \hat{S}_z = \begin{pmatrix} \hat{S}_z & 0 & 0 & 0 \\ 0 & \hat{S}_z & 0 & 0 \\ 0 & 0 & \hat{S}_z & 0 \\ 0 & 0 & 0 & \hat{S}_z \end{pmatrix} = \begin{pmatrix} \frac{1}{2} & 0 & 0 & 0 & 0 \\ 0 & -\frac{1}{2} & 0 & 0 & 0 \\ 0 & 0 & \hat{S}_z & 0 & 0 \\ 0 & 0 & 0 & \hat{S}_z & 0 \\ 0 & 0 & 0 & 0 & \hat{S}_z \end{pmatrix}. \tag{3.6}$$

Generally, a representation of a spin system containing n spins

$$\begin{gathered} \hat{J}_{1z} \to \hat{J}_{1z} \otimes \hat{E}_2 \otimes \hat{E}_3 \otimes \cdots \otimes \hat{E}_n \\ \hat{J}_{2z} \to \hat{E}_1 \otimes \hat{J}_{2z} \otimes \hat{E}_3 \otimes \cdots \otimes \hat{E}_n \\ \vdots \\ \hat{J}_{iz} \to \hat{E}_1 \otimes \cdots \otimes \hat{E}_{i-1} \otimes \hat{J}_{iz} \otimes \hat{E}_{i+1} \otimes \cdots \otimes \hat{E}_n \\ \vdots \\ \hat{J}_{nz} \to \hat{E}_1 \otimes \hat{E}_2 \otimes \cdots \otimes \hat{E}_{n-1} \otimes \cdots \otimes \hat{J}_{nz} \end{gathered} \tag{3.7}$$

The addition of the aforementioned Rb hyperfine coupling requires the insertion of Rb nuclear spin to the spin system. We can determine the dimensions of the composed spin density matrix just from these spins. For example, a spin system consisting of ^{129}Xe nuclear spin ($I_{\mathrm{Xe}} = 1/2$), ^{85}Rb nuclear spin ($I_{\mathrm{Rb}} = 5/2$) and ^{85}Rb electron spin

($S = 1/2$) produce a density matrix with a size of

$$\begin{aligned}[n \times n] &= (2 \times I_{\mathrm{Xe}} + 1) \times (2 \times I_{\mathrm{Rb}} + 1) \times (2 \times S + 1) \\ &= (2 \times 1/2 + 1) \times (2 \times 5/2 + 1) \times (2 \times 1/2 + 1) \\ &= [24 \times 24]\end{aligned} \tag{3.8}$$

We can see that the spin matrix grows with every additional spin introduced in the system. These base spin operators ultimately determine the size of the spin Hamiltonian. However, since the density operator is implicitly tied to the spin Hamiltonian, we can simplify the computation by creating an identity matrix $[\hat{1}]^{n\times n}$ of matching dimensions to $[\hat{H}(t)]^{n\times n}$ and cast it into the Liouvillian as

$$[\hat{\hat{L}}(t)] = -\frac{i}{\hbar}\Big([\hat{1}] \otimes [\hat{H}(t)] - [\hat{H}(t)]^T \otimes [\hat{1}]\Big). \tag{3.9}$$

The exact formal solution of Liouville-von Neumann equation is expressed as

$$\hat{\rho}(t) = e_o^{\int_0^t \hat{\hat{L}}(t')dt'}\hat{\rho}(0), \tag{3.10}$$

where the index o refers to chronological time-ordering and the term $e_o^{\int_0^{t_n} \hat{\hat{L}}(t')dt'}$ stands for time-explicit superpropagator, which we will from now on denote as $\hat{\hat{P}}$. The superpropagator can be expressed as a limited form series expansion with a non-zero timestep δ

$$\hat{\hat{P}}(t) = e_o^{\int_0^{t_n} \hat{\hat{L}}(t')dt'} = \lim_{\delta\to 0} e^{\hat{\hat{L}}(t_n)\delta} \dots e^{\hat{\hat{L}}(t_{k+1})\delta} e^{\hat{\hat{L}}(t_k)\delta} e^{\hat{\hat{L}}(t_{k-1})\delta} \dots e^{\hat{\hat{L}}(t_2)\delta} e^{\hat{\hat{L}}(t_1)\delta}, \tag{3.11}$$

where $t_k = k\delta$. However, in practice it is approximated as

$$\hat{\hat{P}}(t) = e_o^{\int_0^{t_n} \hat{\hat{L}}(t')dt'} \approx e^{\hat{\hat{L}}(t_n)\delta} \dots e^{\hat{\hat{L}}(t_{k+1})\delta} e^{\hat{\hat{L}}(t_k)\delta} e^{\hat{\hat{L}}(t_{k-1})\delta} \dots e^{\hat{\hat{L}}(t_2)\delta} e^{\hat{\hat{L}}(t_1)\delta}, \tag{3.12}$$

where the time-ordering is chronological, meaning that if $t_j > t_i$, $\hat{\hat{L}}(t_j)$ appears to the left relative to $\hat{\hat{L}}(t_i)$. In other words $\hat{\hat{L}}(t_i)$ operates first on the states in the right side [2].

Subject relevant to this thesis is the actual spin polarization transfer from the unpaired spin-polarized Rb electrons to the Xe nuclei. The spin dynamics of an observable $\hat{O}$ can be obtained as a trace

$$O(t) = \frac{Tr[\hat{O}\hat{\hat{P}}(t)\hat{O}]}{\sqrt{Tr(\hat{O}^2)Tr(\hat{O}^2)}} \tag{3.13}$$

where the $\hat{O}$ refers to a specific spin operator and the denominator is a normalization factor. More specifically the z-component polarization transfer from Rb electron to Xe nucleus ($S_z \rightarrow I_z$) gets the form of

$$\mathscr{P}^{\epsilon}_{\hat{S}_z,\hat{I}_z}(t) = I_z(t) = \frac{Tr[\hat{I}_z\hat{\hat{P}}(t)\hat{S}_z]}{\sqrt{Tr(\hat{I}_z^2)Tr(\hat{S}_z^2)}} \tag{3.14}$$

where ϵ refers to a specific collision event. The spin polarization transfer of an ensemble of collision events is described as

$$\mathscr{P}^{total}_{\hat{S}_z,\hat{I}_z}(t) = \sum_{\epsilon} \mathscr{P}^{\epsilon}_{\hat{S}_z,\hat{I}_z}(t), \tag{3.15}$$

where ϵ under the Σ refers to the each individual collision event in the ensemble [2].

Chapter 4

Results and discussion

The presented computations were carried out at static conditions of temperature T, pressure P and external magnetic field. The timestep δ (Eq. 3.12) used in the SD simulations is set to be 50×10^{-15} seconds, or 50 fs. Collision events are divided in discrete categories based on their lifetimes. The term binary collision is used to describe an event where the two collision participants shortly visit each other's proximity, while van der Waals (VDW) complex represents an event where the participants oscillate around each other for at least two times. In the upcoming histograms this is seen as binary collisions being in the bars on the left while the VDW complexes are in the bars on the right. The histograms are represented on a logarithmic scale.

As a function of time, the MD trajectory of a Rb atom in Xe gas was simulated conforming to $T = 300$ K and $p = 2.4$ bar. The interaction events of the Rb-Xe pairs were extracted from constant $\delta = 50$ fs SD snapshots. Produced binary data is fed into the python code via the MDanalysis package to perform the SD simulations. Based on QC calculations, using relativistic density-functional theory, instantaneous parameters ($\boldsymbol{A}(t)$, $\boldsymbol{g}(t)$) of the spin Hamiltonian were constructed. With the parameters at hand for SD, a time series of spin Hamiltonians for every Rb-Xe interaction is forged in order to propagate the spin density matrix forward and ultimately simulate the polarization transfer from the unpaired Rb electron to the Xe nuclei.

4.1 Polarization transfer to ^{129}Xe and ^{131}Xe

With our method we have simulated the total spin polarization transfer of an ensemble of 14603 collision events, divided into categories based on their lifetimes. In these results, the terms of our spin Hamiltonian are $\hat{H}(t) = \mu_B \hat{\boldsymbol{S}} \cdot \boldsymbol{g}(t) \cdot \boldsymbol{B} + \hat{\boldsymbol{S}} \cdot \boldsymbol{\epsilon}(t) \cdot \boldsymbol{M} + \hat{\boldsymbol{S}} \cdot \boldsymbol{A}_{\mathrm{Xe}}(t) \cdot \hat{\boldsymbol{I}}_{\mathrm{Xe}}$.

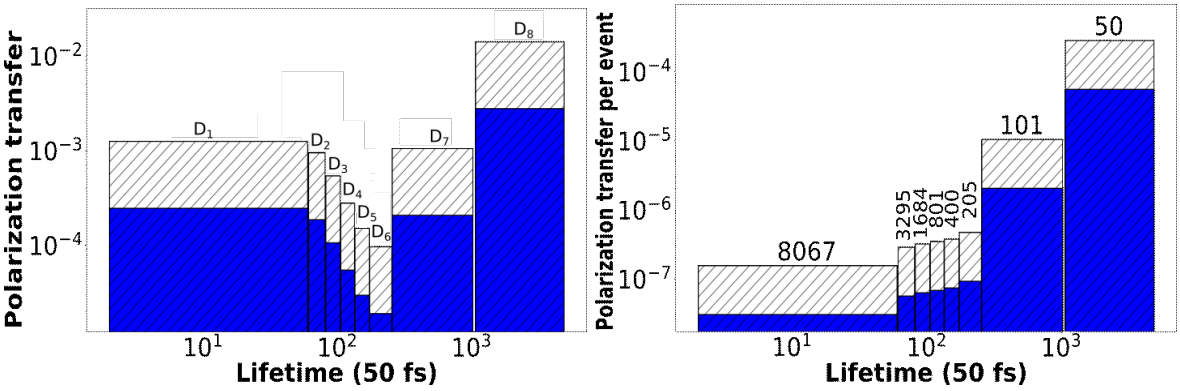

Figure 4.1: Histograms of the spin polarization transfer from ^{85}Rb electrons to $^{129/131}$Xe nuclei ($S_z \rightarrow I_z$) divided into categories determined by collision event duration. On the left histogram, D_r above the bars refers to a specific category of events. The ordering of these categories stays the same on all of the upcoming histograms. Numbers on top of the right histogram represent the number of events in that category. On the left we have the total polarization transfers and on the right the polarization transfers averaged with the number of collision events per section, with white and blue representing the polarization transfer to ^{129}Xe and ^{131}Xe, respectively. The propagator used is (3.12).

Figure 4.1 shows that achieved polarization transfers are far less for ^{131}Xe than for ^{129}Xe, just as expected [12]. The unique gyromagnetic ratio of ^{131}Xe being weaker than ^{129}Xe ($2.209076 \times 10^7 \frac{rad}{Ts}$ and $-7.452103 \times 10^7 \frac{rad}{Ts}$) also gave a strong clue in the expectancy of these results. It is important to note that for the simulated ^{131}Xe polarization transfers, new MD trajectories were not calculated because of the expected near-zero impact on the results due to the small percentual mass difference of ^{129}Xe and ^{131}Xe. The polarization transfer results of ^{129}Xe are in accordance with previous model of this simulation [13].

Table 4.1: Table of ^{129}Xe and ^{131}Xe averaged polarisation transfer values from the histogram above (Fig. 4.1) categorized by the respective D_r. Percentual differences (^{131}Xe/^{129}Xe) of these values are calculated in the rightmost column.

Averaged polarization transfers (pol. transfer per event)				
Category	Number of events	^{129}Xe (white)	^{131}Xe (blue)	$\frac{\mathscr{P}(^{131}\mathrm{Xe})}{\mathscr{P}(^{129}\mathrm{Xe})} \times 100\%$
D_8	50	2.831×10^{-4}	5.563×10^{-5}	19.650%
D_7	101	1.047×10^{-5}	2.058×10^{-6}	19.656%
D_6	205	4.717×10^{-7}	9.274×10^{-8}	19.660%
D_5	400	3.779×10^{-7}	7.429×10^{-8}	19.659%
D_4	801	3.482×10^{-7}	6.844×10^{-8}	19.655%
D_3	1684	3.216×10^{-7}	6.319×10^{-8}	19.649%
D_2	3295	2.885×10^{-7}	5.667×10^{-8}	19.643%
D_1	8067	1.558×10^{-7}	3.059×10^{-8}	19.634%

It is interesting to note that the polarization transfer efficiency in the case of ^{131}Xe

versus ^{129}Xe decreases by a nearly uniform percentage in all categories of event lengths.

4.2 Effect of hyperfine coupling to Rb nucleus

Including the hyperfine coupling of rubidium electron and nuclear spins requires the addition of spin Hamiltonian term $\hat{\boldsymbol{S}} \cdot \boldsymbol{A}_{\mathrm{Rb}}(t) \cdot \hat{\boldsymbol{I}}_{\mathrm{Rb}}$. With this term included, we can see the results illustrated in Fig. 4.2.

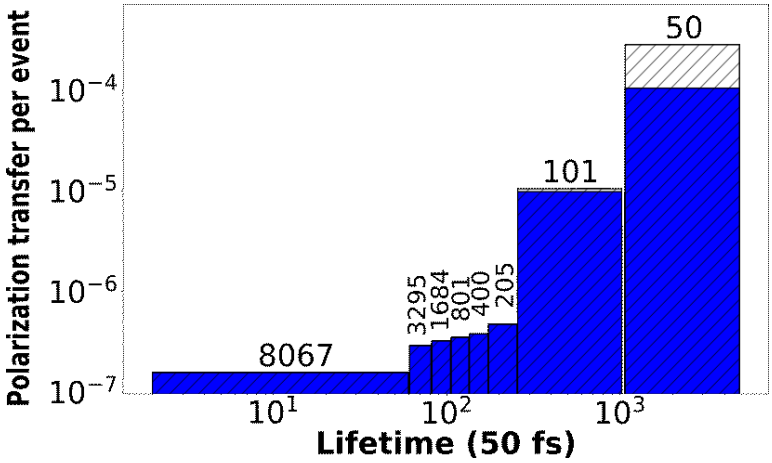

Figure 4.2: Averaged histogram of spin polarization transfer from ^{85}Rb to ^{129}Xe ($S_z \rightarrow I_z$) with hyperfine coupling of rubidium electron spin to its own nuclear spin included represented in the blue bars. On the white bars we have comparison results without the hyperfine interaction. The propagator used is (3.12).

Table 4.2: Table of ^{129}Xe averaged polarisation transfer with and without the Rb hyperfine coupling (HFC) from the histogram above (Fig. 4.2) categorized by the respective D_r in the same way as presented in Fig. (4.1). Percentual differences of these values are calculated in the rightmost column.

Averaged polarization transfers (pol. transfer per event)				
Category	Number of events	Without HFC (white)	HFC included (blue)	$\frac{\mathscr{P}(With\,HFC)}{\mathscr{P}(No\,HFC)} \times 100\%$
D_8	50	2.831×10^{-4}	1.046×10^{-4}	36.948%
D_7	101	1.047×10^{-5}	9.802×10^{-6}	93.620%
D_6	205	4.717×10^{-7}	4.702×10^{-7}	99.682%
D_5	400	3.779×10^{-7}	3.774×10^{-7}	99.868%
D_4	801	3.482×10^{-7}	3.479×10^{-7}	99.914%
D_3	1684	3.216×10^{-7}	3.214×10^{-7}	99.938%
D_2	3295	2.885×10^{-7}	2.883×10^{-7}	99.931%
D_1	8067	1.558×10^{-7}	1.557×10^{-7}	99.936%

We can see that the addition of Rb hyperfine coupling has most effect in the longest VDW collisions, where it disrupts the flow of spin transfer. However, the negative impact drops off quickly as event durations decrease, and is effectively zero in the binary collisions. A closer look into traces of individual collision events gives us insight on the matter.

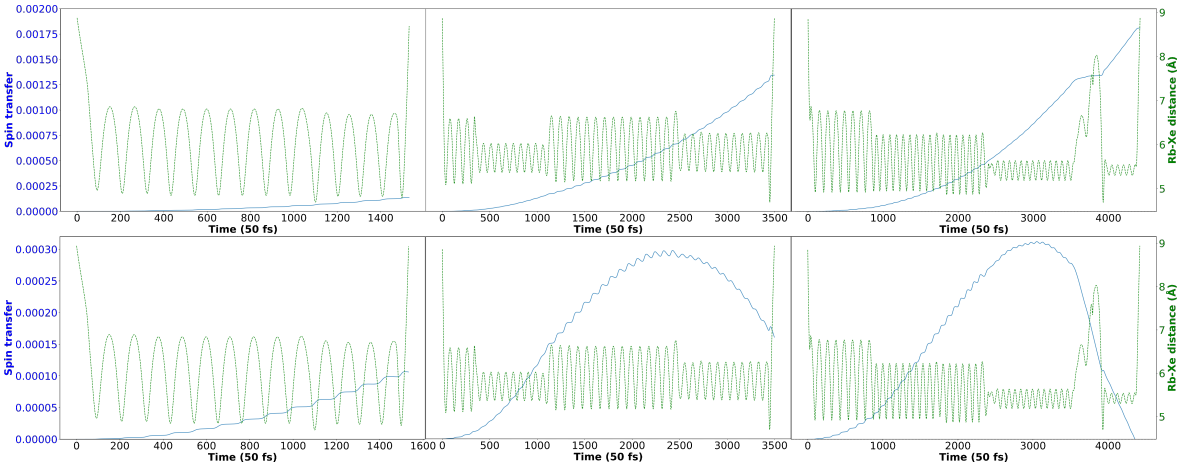

Figure 4.3: Singular VDW interaction events picked from the ensemble. On the y-axis we have two different values, blue and green. Blue refers to the spin transfer from ^{85}Rb to ^{129}Xe ($S_z \rightarrow I_z$), green expresses the distance between the two atoms during the collision. Time is on the x-axis. We have two rows of figures with three different traces of events with varying collision duration. On the top row are the traces without hyperfine coupling to ^{85}Rb nucleus, while on the bottom row the same collision events with hyperfine coupling included.

Figure 4.3 shows examples of individual VDW interaction events, with and without the rubidium hyperfine coupling. We can see that with the addition of hyperfine coupling, the spin transfer doesn't necessarily increase with collision duration anymore. After a certain lifetime, the polarization transfer starts to decline. In the longest of the selected events it can even achieve negative transfer, meaning spin polarization was lost. Additionally, fluctuations in the Rb-Xe distance of during the oscillation of the VDW complex seem to change the shape of the spin transfer steps illustrated in the blue graphs. When the Rb-Xe pair is far apart, the achieved transfer bleeds back through the hyperfine coupling of the Rb nucleus. This also happens in the shorter distances but it is not noticeable, since the spin transfer towards Xe is greater.

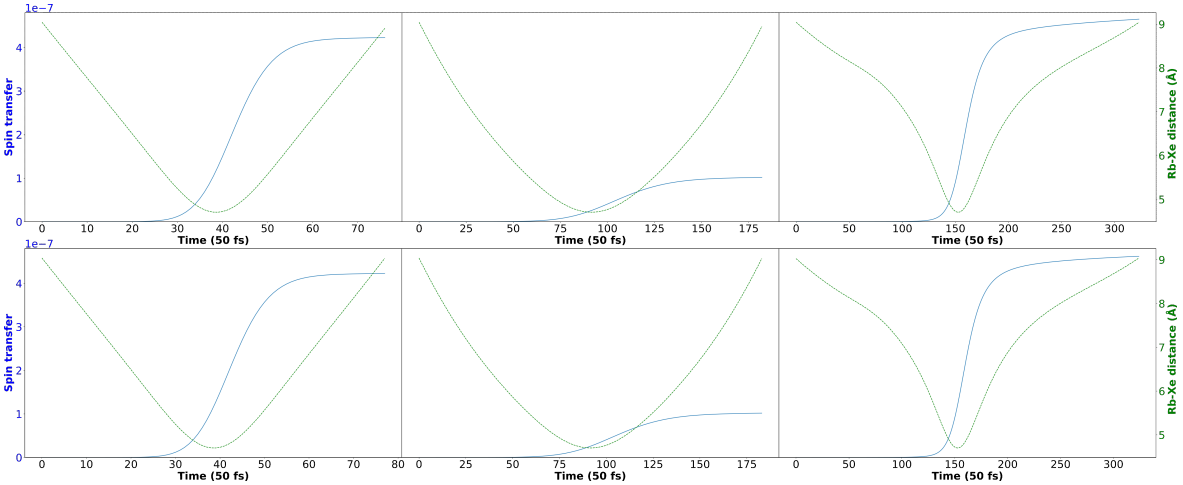

Figure 4.4: Singular binary interaction events picked from the ensemble. The axes have the same variables as in Fig (4.3). There are two rows of figures with three different traces of events with varying collision duration. On the top row are the traces without hyperfine coupling to ^{85}Rb nucleus, while on the bottom row the same collision events with hyperfine coupling included.

Figure 4.4 shows three selected individual binary collision events from the ensemble. We can clearly see that the addition of the Rb hyperfine coupling has effectively no impact on the shorter-duration interaction events. There is no time to bleed out the spin transfer without the oscillation of the Rb-Xe pair, contrary to the longer VDW complexes. The spin transfer of the binary collisions remain nearly unchanged, just as was to be expected from the results seen in Fig. (4.2).

4.3 Rate of polarization transfer

Spin transfers of individual events are divided by their lifetimes to reveal how quickly spin is transferred, or rather what the rate of spin transfer is. Doing this for the whole ensemble gives us a vision how collision duration relates with the rate of polarization transfer. In practice this is done by first calculating the spin transfer of each individual event in the ensemble and dividing it by its lifetime, then separating them into their respective categories and finally dividing, or rather averaging, said category by the number of its events N_r:

$$\left\langle \frac{d\mathscr{P}^{r}_{\hat{S}_z,\hat{I}_z}}{dt} \right\rangle = \frac{1}{N_r} \sum_{\epsilon} \frac{\mathscr{P}^{\epsilon}_{\hat{S}_z,\hat{I}_z}}{\tau^{\epsilon}}. \tag{4.1}$$

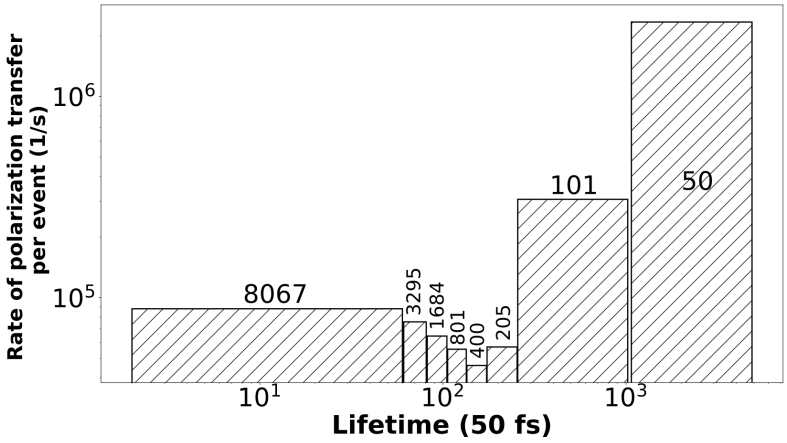

Figure 4.5: Rate of polarization transfer from ^{129}Xe to ^{85}Rb ($S_z \rightarrow I_z$) averaged by the number of events per category, calculated according to Eq. (4.1), using the spin Hamiltonian $\hat{H}(t) = \mu_B \hat{\boldsymbol{S}} \cdot \boldsymbol{g}(t) \cdot \boldsymbol{B} + \hat{\boldsymbol{S}} \cdot \boldsymbol{\epsilon}(t) \cdot \boldsymbol{M} + \hat{\boldsymbol{S}} \cdot \boldsymbol{A}_{\mathrm{Xe}}(t) \cdot \hat{\boldsymbol{I}}_{\mathrm{Xe}}$.

Figure 4.5 shows the averaged rate of polarization transfer per category of collisions for the ensemble. Without the addition of the aforementioned ^{85}Rb hyperfine coupling, a correlation between the rate of transfer and event duration is visible. A slight dip in the medium duration events is noticeable, yet the results indicate that the longer-lived collisions seem to transfer spin more rapidly. The rate of polarization transfer appears to increase exponentially as a function of the event lifetime.

However, with the addition of the Rb hyperfine coupling we can see how the longest duration events take a dive in the sense of transfer rate as shown in Fig (4.6).

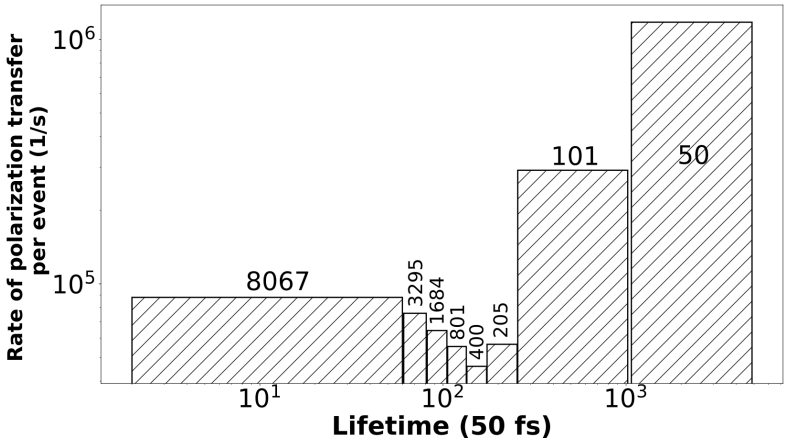

Figure 4.6: Rate of polarization transfer from ^{129}Xe to ^{85}Rb ($S_z \rightarrow I_z$) averaged by the number of events per category, calculated according to Eq. (4.1). With the Rb hyperfine coupling included, the spin Hamiltonian terms used are $\hat{H}(t) = \mu_B \hat{\boldsymbol{S}} \cdot \boldsymbol{g}(t) \cdot \boldsymbol{B} + \hat{\boldsymbol{S}} \cdot \boldsymbol{\epsilon}(t) \cdot \boldsymbol{M} + \hat{\boldsymbol{S}} \cdot \boldsymbol{A}_{\mathrm{Xe}}(t) \cdot \hat{\boldsymbol{I}}_{\mathrm{Xe}} + \hat{\boldsymbol{S}} \cdot \boldsymbol{A}_{\mathrm{Rb}}(t) \cdot \hat{\boldsymbol{I}}_{\mathrm{Rb}}$.

Figure 4.6 reveals the effect of the Rb hyperfine coupling in the polarization transfer

of the ensemble. Although a similar correlation between event duration and the rate of transfer seems to hold, the polarization transfer in the longest collision event categories has decreased substantially, as was to be expected from the individual investigation of the VDW events seen in Fig. (4.3). This decrease is negligible in the shorter duration categories. The rubidium hyperfine coupling seems to determine a definite limit to how long a collision event can optimally be before it starts to lose efficiency. However, the probability of events of this length can be manipulated with conditions. Further research into the subject is needed.

Chapter 5

Conclusions

Nuclear spins are intrinsically linked to NMR spectroscopy. The strength of NMR signal is determined by the net magnetization of a sample, which is regulated by the differences in nuclear spin state occupations. These occupations can be devised beyond thermal equilibrium with specific procedures known generally as hyperpolarization techniques. One of the currently relevant techniques is spin-exchange optical pumping, which can provide great benefits in NMR spectroscopy. However, the technique has not yet been completely exhausted and pressing questions still remain concerning its optimization.

As an approach to this optimization, a multi-scale simulation was created, combining efforts of molecular dynamics, quantum chemistry and spin dynamics. It is used to model spin polarization exchange between alkali-metal electrons and noble-gas nuclei in gas-phase collisions. With this method, microscopic examination of individual collision events can be achieved. Quantitative analysis can be carried out with an ease of changing the environmental conditions as well as the interaction parameters.

Through the propagation of spin density matrix, more and less expected results were seen. The polarization transfer to the ^{131}Xe isotope was found to be less than its counterpart, ^{129}Xe. This was anticipated based on former research done in the field. However, the nearly uniform percentual difference over the distinct event duration categories was surprising. With the addition of the hyperfine coupling to the Rb nucleus, the polarization transfer to ^{129}Xe decreased. It appears the long-lived van der Waals complexes face the most negative impacts in the polarization transfer, while the short binary collisions remain effectively unchanged. In the individual VDW complexes, spin transfer steps start to deform and the transfer bleeds away to Rb. The most extreme cases show that even a negative spin transfer is possible, meaning spin transfer to Xe nuclei was lost. This implies that there is a limit to how long the collisions can get before losing effectiveness. Nontheless, the probability of event duration distribution can be manipulated with conditions such as gas pressure and temperature.

The simulation method offers benefits over the experimental approach, but still needs refinement. Development potential can be found immediately with the addition

of more terms to the spin Hamiltonian, such as the ^{131}Xe quadrupolar coupling and Rb-Xe dipolar coupling. However, these are yet to be implemented and their effects studied. Further research is to be expected in near future.

Bibliography

[1] T. G. Walker & W. Happer: Spin-exchange optical pumping of noble-gas nuclei, *Rev. Mod. Phys.* **69**, (1997), 629–642.

[2] J. Rantaharju: *Magnetization dynamics in paramagnetic systems*, PhD thesis, University of Oulu, (2018)

[3] J. Rantaharju, J. Mareš, & J. Vaara: Spin dynamics simulation of electron spin relaxation in Ni^{2+}(aq), *J. Chem. Phys.* **141**, (2014), 014109.

[4] V.-V. Telkki: *Spektroskooppiset menetelmät, NMR-spektroskopia*, University of Oulu, lecture material, (2015)

[5] J. P. Hornak: *The Basics of NMR*, [Online; 26.2.2015], (2011)

[6] D. A. Barskiy, *et al.*: NMR hyperpolarization techniques of gases, *Chemistry*, **23**, (2017), 725–751.

[7] D. M. L. Lilburn, G. E. Pavlovskaya, & T. Meersmann: Perspectives of hyperpolarized noble gas MRI beyond ^{3}He, *J. Magn. Reson.* **229**, (2013), 173–186.

[8] J. E. Harriman: *Theoretical foundations of electron spin resonance*, Academic Press, (1978)

[9] J. R. F. Curl: The relationship between electron spin rotation coupling constants and g-tensor components, *Mol. Phys.* **9**, (1965), 585–597.

[10] J. Tuorila: *Kvanttimekaniikka I*, University of Oulu, lecture material, (2017)

[11] H. P. Breuer & F. Petruccione: *The theory of open quantum systems*, Oxford University Press, (2002)

[12] K. F. Stupic, Z. I. Cleveland, G. E. Pavlovskaya, & T. Meersmann: Hyperpolarized ^{131}Xe NMR spectroscopy, *J. Magn. Reson.* **208**, (2011), 58–69.

[13] J. Rantaharju, M. Hanni, & J. Vaara: *Polarization transfer in spin-exchange optical pumping experiment*, submitted for publication.

[14] J. Rantaharju & J. Vaara: Liquid-state paramagnetic relaxation from first principles, *Phys. Rev. A*, **94**, (2016), 043413.